Tuning interfacial domain walls in GdCo/Gd/GdCo′ spring magnets

C. Blanco-Roldán,[1,2] Y. Choi,[3] C. Quirós,[1,2] S. M. Valvidares,[4] R. Zarate,[1] M. Vélez,[1,2]
J. M. Alameda,[1,2] D. Haskel,[3] and J. I. Martín[1,2,*]

[1]*Dpto. Física, Universidad de Oviedo, 33007 Oviedo, Spain*

[2]*Centro de Investigación en Nanomateriales y Nanotecnología-CINN (Consejo Superior de Investigaciones Científicas CSIC-Universidad de Oviedo), 33940 El Entrego, Spain*

[3]*Advanced Photon Source, Argonne National Laboratory, Argonne, Illinois 60439, USA*

[4]*ALBA Synchrotron Light Facility, Carrer de la Llum 2-26, 08290 Cerdanyola del Vallès, Barcelona, Spain*

Spring magnets based on GdCo multilayers have been prepared to study the nucleation and evolution of interfacial domain walls (iDWs) depending on layer composition and interlayer coupling. GdCo alloy compositions in each layer were chosen so that their net magnetization aligns either with the Gd ($Gd_{35}Co_{65}$) or Co($Gd_{11}Co_{89}$) sublattices. This condition forces an antiparallel arrangement of the layers' net magnetization and leads to nucleation of iDWs above critical magnetic fields whose values are dictated by the interplay between Zeeman and exchange energies. By combining x-ray resonant magnetic scattering with Kerr magnetometry, we provide detailed insight into the nucleation and spatial profile of the iDWs. For strong coupling (GdCo/GdCo′ bilayer), iDWs are centered at the interface but with asymmetric width depending on each layer magnetization. When interlayer coupling is weakened by introducing a thin Gd interlayer, the exchange spring effect becomes restricted to a lower temperature and field range than observed in the bilayer structure. Due to the ferromagnetic alignment between the high magnetization $Gd_{35}Co_{65}$ layer and the Gd interlayer, the iDW shrinks and moves into the lower exchange Gd interlayer, causing a reduction of iDW energy.

PACS number(s): 75.60.Ch, 75.70.Cn, 75.50.Kj

I. INTRODUCTION

Exchange coupled multicomponent systems that combine ferrimagnetic and ferromagnetic materials are the focus of a renewed interest due to their potential as recording media with tailored magnetic behavior [1]. Different geometries such as thin film multilayers [2], core-shell nanoparticles [3], or hard/soft lateral nanocomposites [4] are employed in order to optimize system properties for specific applications. Heterostructures provide an opportunity to design materials with improved properties by combining materials with dissimilar properties [1–12]. For example in exchange-spring permanent magnets [7], combination of magnetically soft and hard materials leads to a composite permanent magnet with an energy product higher than those of constituent materials.

A general characteristic of magnetic heterostructures is the crucial role of interfacial coupling between different layers in determining overall properties [5–8,11–14]. Thus, detailed characterization and understanding of the interfacial coupling and interfacial magnetization configuration are essential in guiding material design. In particular, in the case of exchange coupled multilayers, exchange springs are often found in the magnetization reversal process, i.e., interfacial domain walls (iDWs) at the boundary between different materials in which the magnetization rotates gradually across the wall thickness due to the combined effect of interfacial exchange coupling, magnetic anisotropies, and applied field. Understanding exchange springs and iDWs is essential to determine the magnitude of exchange bias in thin ferromagnetic/antiferromagnetic bilayers [5], to tune giant magnetoresistance in spin valves

[6], to optimize magnetic recording media [7,8], or even to determine exchange stiffness constants in thin film systems [9]. Thus, there are recent efforts to improve the microscopic characterization of magnetization profiles of iDWs in spring magnets both with neutron and x-ray resonant magnetic scattering (XRMS) techniques [8,10–12]. In turn, as iDW magnetization profiles become more accurately described, the relevance of thin interlayers in the complexity of the global reversal process becomes evident [11–14], i.e., changes in interface properties that modify iDW profiles appear as key parameters to tailor the magnetic behavior of the system.

Spring magnets have been widely studied in exchange coupled multilayers of amorphous ferrimagnetic rare earth (*Re*)-transition metal (TM) alloys. In these systems, nucleation/annihilation processes of iDWs can be easily controlled by properly tuning the magnetic properties of each layer in the system with composition and/or temperature [15,16]. As a result, different magnetic responses have been produced, such as macroscopic ferrimagnet states [17], macroscopic spin-flip-like metamagnetic states [18], or giant exchange bias [2]. In particular, Gd-Co amorphous alloys are a very simple *Re*-TM ferrimagnetic material where the Gd and Co moments are antiferromagnetically coupled and collinear [19]. Depending on the composition and temperature, the net magnetization in these alloys can be aligned either with the Co or the Gd moments. Therefore, it is possible to prepare exchange coupled Gd-Co/Gd-Co′ bilayers with different composition so that the net magnetization in each layer is dominated by a different kind of magnetic moments (i.e., by the Gd or Co moments). As sketched in Fig. 1, interfacial exchange coupling between Co atoms at each layer results in the antiparallel alignment of the magnetization in each layer at remanence. Then, under an in-plane magnetic field of increasing magnitude, the system
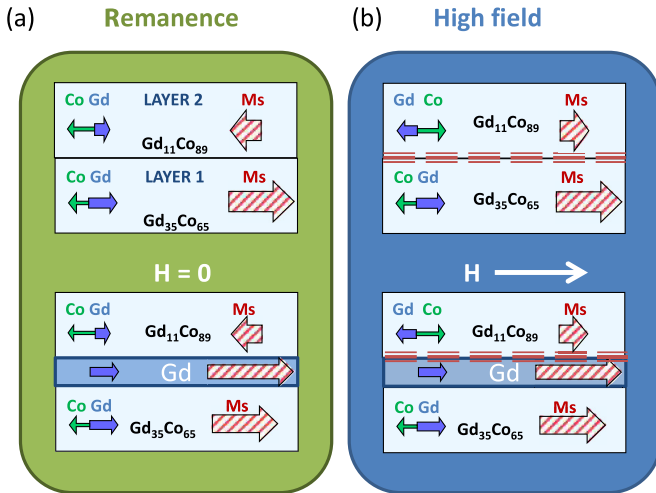
*jmartin@uniovi.es

FIG. 1. (Color online) Sketch of the magnetic configuration of Gd-Co/Gd-Co′ bilayers and Gd-Co/Gd/Gd-Co′ trilayers at remanence (a) and at a high field (b). Dashed line indicates iDW at high field.

must switch to a parallel magnetization configuration, and an iDW is created at the interface.

In this paper, we demonstrate how the spring magnet effect can be tuned in exchange coupled GdCo multilayers when iDWs are modified playing with layer composition and interlayer coupling. Thin, soft Gd interlayers have been added at the interface of GdCo/Gd/GdCo′ multilayers, and the location and detailed structure of the buried iDW have been studied by depth- and element-resolved magnetic characterization with XRMS measurements. For strong coupling (no Gd interlayer), iDWs are centered at the system interface with an asymmetric DW width. As coupling is reduced, the iDW shrinks and shifts from the largest magnetization GdCo layer into the Gd interlayer in which a significant fraction of the magnetization rotation takes place. The weaker exchange interactions within this central Gd layer reduce iDW energy, and, as a consequence, the transitions between antiparallel coupling and spring magnet states become restricted to a lower field and temperature range.

II. EXPERIMENTAL

The *Re*-TM amorphous alloy multilayers, $Gd_{35}Co_{65}/Gd/Gd_{11}Co_{89}$, have been grown by dc magnetron sputtering on quartz substrates covered by a 10 nm thick Al buffer layer [18]. The alloys were deposited at room temperature at an Ar pressure of 10^{-3} Torr from high purity Co and Gd targets. The composition of the layers can be varied by controlling the relative powers of both sputtering guns: the compositions of the top/bottom alloy layers are $Gd_{11}Co_{89}$ and $Gd_{35}Co_{65}$, respectively, chosen so that the total magnetic moment of each layer is dominated by a different magnetic atom sublattice (Gd at the bottom $Gd_{35}Co_{65}$ layer and Co at the top $Gd_{11}Co_{89}$ layer) in the whole temperature range studied (50 K–300 K) (see sketch in Fig. 1). In the following, the bottom $Gd_{35}Co_{65}$ layer will be labeled as Layer 1, and the top $Gd_{11}Co_{89}$ layer will be labeled as Layer 2. The amorphous structure of the bilayers has been verified by x-ray diffraction. Both Gd-Co layers

have the same nominal thickness $t_1 = t_2 = 50$ nm, whereas the thickness of the intermediate Gd layer has been varied from $t_{Gd} = 0-15$ nm. The samples are *in situ* covered with a 10 nm thick Al layer to avoid oxidation.

The magnetic characterization has been performed by SQUID magnetometry to obtain the net magnetization $M_S(T)$ of single layers of the Gd-Co alloys [20]. Magneto-optical transverse Kerr effect (MOTKE) with white light has been used to analyze magnetization reversal processes in the bilayer/trilayer samples [18]. MOTKE is particularly useful for two reasons: the short penetration depth of visible light in these alloys (around 40 nm, i.e., shorter than each layer thickness [21]) and the sensitivity of the Kerr signal in the visible range only to the magnetic behavior of the Co sublattice and not to the Gd moments contribution [22]. Thus, MOTKE hysteresis loops provide the magnetic behavior of only the Co sublattice in either the top or bottom Gd-Co layer depending on whether the incident light enters the sample from the top or bottom surface [18]. The samples present a small in-plane uniaxial anisotropy that is defined by the oblique incidence of the atoms during the off-normal deposition, and the magnetic field (H) has always been applied in the sample plane along the easy axis of these uniaxial systems [18].

In the studied field range, H up to 10 kOe, it is possible to assume the antiparallel alignment of Gd and Co moments since J_{AF}, exchange coupling between Co and Gd spins, is large enough in comparison with Zeeman energy ($J_{AF} = -2.1 \times 10^{-15}$ erg [19,23] and $\mu_B H = 9.2 \times 10^{-17}$ erg with μ_B, the Bohr magneton, and $H = 10$ kOe). In general, a large enough magnetic field could modify the exchange induced antiparallel alignment between Co and Gd moments, and its effect should be largest within the iDW at the points where the magnetization is perpendicular to the applied field and field induced torque is maximum. In this case, a simple estimate of $\Delta\theta$, the field induced rotation of Co and Gd spins (S_{Co} and S_{Gd}) towards the magnetic field [24], gives $\Delta\theta = g\mu_B H(S_{Co} + S_{Gd})/(4 J_{AF} S_{Co} S_{Gd})$. For $g = 2$, $S_{Co} = 2$, $S_{Gd} = 7/2$ and $H = 10$ kOe (the maximum field used), $\Delta\theta$ is just 0.017 rad. Thus, as a first approximation, this deviation has been neglected, and the magnetization of Co and Gd sublayers has been considered antiparallel in the studied field range.

Figure 2 shows the temperature dependence of the net saturation magnetization $M_S(T)$ for two single 50 nm thick $Gd_{35}Co_{65}$ and $Gd_{11}Co_{89}$ layers [Fig. 2(a)] and their corresponding MOTKE loops at 50 K [$Gd_{35}Co_{65}$ layer in Fig. 2(b) and $Gd_{11}Co_{89}$ layer in Fig. 2(c)]. The M_S, measured by SQUID, includes the contribution of both the Gd and Co atoms in each alloy. Figure 2(a) shows a monotonous trend in $M_S(T)$ for both Gd-Co alloys, indicating that there are no compensation temperatures and that the same sublattice dominates the magnetization in each case over the whole temperature range of the measurement (Gd in $Gd_{35}Co_{65}$ and Co in $Gd_{11}Co_{89}$). The MOTKE loops, only sensitive to the Co sublattice, allow us to determine the dominant ion sublattice in each case: Kerr signal at saturation is negative for $Gd_{35}Co_{65}$ [Fig. 2(b)] and is positive for $Gd_{11}Co_{89}$ [Fig. 2(c)]. This indicates that the net magnetization is aligned with a different ion sublattice in each case, as sketched in the insets of Fig. 2: M_S is aligned with Gd sublattice for $Gd_{35}Co_{65}$ (thus, due to the antiferromagnetic Gd-Co coupling, Co
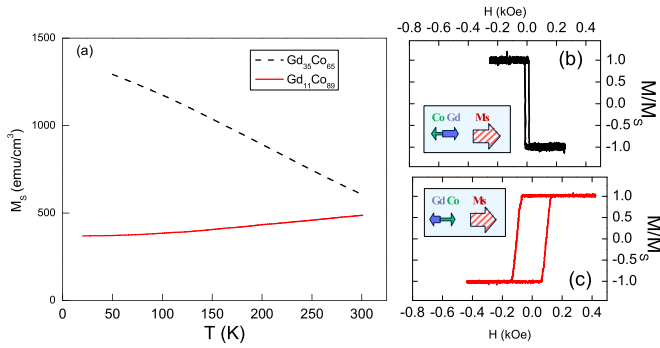
FIG. 2. (Color online) (a) Temperature dependence of the saturation magnetization of 50 nm thick Gd-Co single films with different compositions. MOTKE hysteresis loops are shown for (b) $Gd_{35}Co_{65}$ and (c) $Gd_{11}Co_{89}$ at 50 K. Note that at this wavelength, the magneto-optical signal comes exclusively from the Co sublattice: the inverted loop observed for $Gd_{35}Co_{65}$ corresponds to an alloy with net magnetization dominated by the Gd sublattice whereas the direct loop observed for $Gd_{11}Co_{89}$ corresponds to an alloy with magnetization dominated by the Co sublattice (see sketches in the insets).

magnetization is oriented opposite to the applied field and the Kerr signal is negative), and M_S is aligned with Co sublattice for $Gd_{11}Co_{89}$, resulting in a positive Kerr signal at saturation.

For Gd-resolved magnetic characterization, XRMS measurements where performed in a longitudinal geometry at beamline 4-ID-D of the Advanced Photon Source, Argonne National Laboratory [25,26]. A split-coil, cryogenic superconducting magnet mounted on a Huber diffractometer provided tunable magnetic fields along the incident x-ray wave vector. The sample was cooled independently with a closed cycle cryostat inserted in the room temperature bore of the magnet. Circularly polarized x-rays were produced with phase retarding optics. The XRMS measurements were done by switching x-ray helicity at each angular position along the specular reflectivity curves. Measurements were repeated with magnetic field opposite the incident x-ray wave vector to check for experimental artifacts. Reflectivity was measured using a horizontal scattering geometry. Complex resonant scattering factors at the Gd L_3 edge, $f_1 + i f_2$, were obtained by measuring the x-ray absorption of a $Gd_{11}Co_{89}$ single layer sample in fluorescence mode, scaling to Henke's f_2 tabulated values [27], and using a Kramers-Kronig transformation to obtain the real part of the scattering factor, f_1. Energy was fixed to near the Gd L_3 absorption edge, $E = 7245$ eV. Temperature was fixed to 50 K and magnetic fields of increasing magnitude were applied along the easy axis of the samples to alter the magnetization depth profile (either with or without iDW). The corresponding changes in the depth profile of Gd magnetic moments will be detected in the XRMS scans.

Figure 3 shows XRMS chemical (charge) reflectivity data (obtained from the average of reflectivity curves measured with opposite x-ray helicity, $[I(C+) + I(C-)]/2$) for a 50 nm $Gd_{35}Co_{65}/50$ nm $Gd_{11}Co_{89}$ bilayer at $H = 0.2$ kG, showing well defined low angle oscillations. These data have been fitted using Pythonic Programming for Multilayers (PPM) code [28] in order to obtain a good structural description of the samples. The obtained chemical profiles have then been
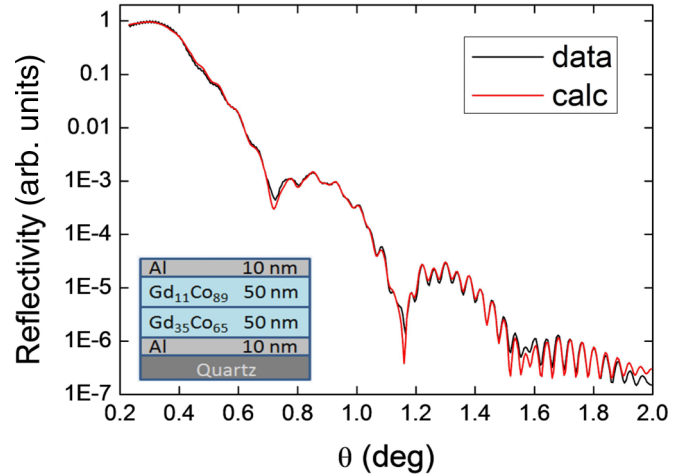

FIG. 3. (Color online) Resonant small angle x-ray reflectivity measured in a longitudinal geometry at $E = 7245$ eV (Gd L3 edge) for a 50 nm $Gd_{35}Co_{65}/50$ nm $Gd_{11}Co_{89}$ bilayer. Red lines are structural fits with PPM code.

used as a basis for the analysis of the magnetization depth profiles from the fits of the low angle resonant asymmetry ratio $[I(C+) - I(C-)]/[I(C+) + I(C-)]$. Each layer in the system is characterized by its density ρ_i, thickness t_i, and Gaussian roughness r_i. Densities are fixed at their nominal values, whereas layer thickness and roughness are allowed to vary in order to obtain the best fit of the reflectivity data. Alloy densities are calculated from the average of pure Co and Gd densities taking into account their nominal atomic composition. Thus, $\rho_1 = 8.55$ g/cm^3, $\rho_2 = 8.79$ g/cm^3, and $\rho_{Gd} = 8.38$ g/cm^3. Fitted structural parameters are $t_1 = 51.4$ nm and $t_2 = 49.3$ nm (in agreement with the nominal 50 nm value) with a Gaussian roughness $r_1 = 1.4$ nm and $r_2 = 1.3$ nm for each layer. The results of a similar fit for the low angle reflectivity data of a 50 nm $Gd_{35}Co_{65}/7.5$ nm Gd/50 nm $Gd_{11}Co_{89}$ trilayer are $t_1 = 52.5$ nm, $t_2 = 48.5$ nm, and $t_{Gd} = 8.3$ nm with Gaussian roughness $r_1 = 2.0$ nm, $r_2 = 1.3$ nm, and $r_{Gd} = 1.5$ nm, respectively.

III. RESULTS AND DISCUSSION

A. Magnetization reversal process in GdCo/Gd/GdCo′ trilayers

Magnetization reversal in exchange coupled Gd-Co/Gd-Co′ bilayers takes place through a series of transitions that are driven by the competition between Zeeman energy (that tends to align the net magnetic moment of each layer with the field) and interfacial exchange (that favors the parallel alignment of Co magnetic moments at the interface) [29]. Depending on the net magnetic moment of each layer and the dominant magnetic ion sublattice in each of them, these transitions may involve the nucleation/annihilation of iDWs [18]. This can be seen, for example, in the MOTKE loops measured at different temperatures for the 50 nm $Gd_{35}Co_{65}/50$ nm $Gd_{11}Co_{89}$ bilayer with incident light at the top sample surface [Figs. 4(a-c)]. In this case, the MOTKE signal comes mainly from the Co sublattice of the top $Gd_{11}Co_{89}$ layer (Layer 2) that, according to the results in Fig. 2(b), is aligned with the total magnetization of this layer.

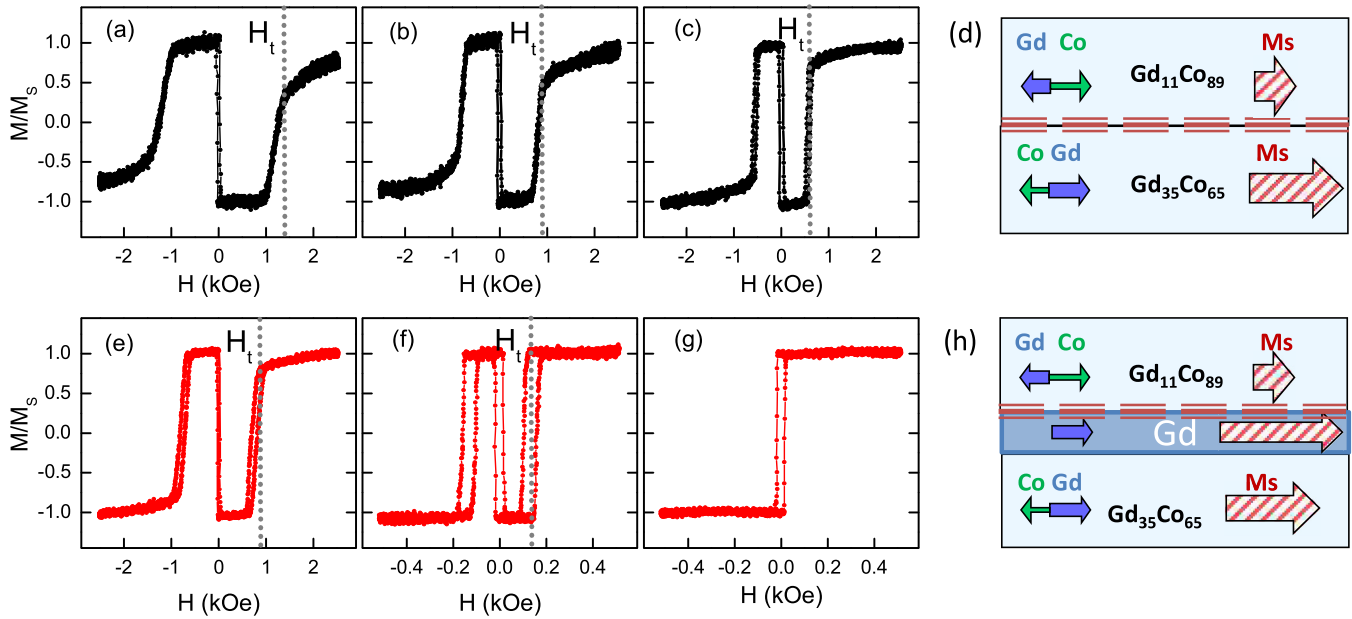FIG. 4. (Color online) MOTKE hysteresis loops of top $Gd_{11}Co_{89}$ layer (Layer 2) for a 50 nm $Gd_{11}Co_{89}$/50 nm $Gd_{35}Co_{65}$ bilayer at (a) 50 K, (b) 150 K, and (c) 200 K and for a 50 nm $Gd_{11}Co_{89}$/7.5 nm Gd/50 nm $Gd_{35}Co_{65}$ trilayer at (e) 50 K, (f) 150 K, and (g) 200 K. Dotted lines indicate H_t, the transition field for Layer 2. (d), (h) Sketches of the magnetization configuration of the samples at high field, indicating the relative orientation of Gd and Co sublattices in each case. Thick dashed line indicates the iDW.

At high fields, Zeeman energy dominates, and the net magnetization of both Layer 1 ($Gd_{35}Co_{65}$) and Layer 2 ($Gd_{11}Co_{89}$) should be aligned with the field. However, as sketched in Fig. 4(d), this implies the presence of an iDW at the boundary between both layers due to the different alignment of Co sublattices with the net magnetization in each case (antiparallel in Layer 1 and parallel in Layer 2), i.e., the bilayer behaves as an exchange spring. As the magnitude of the applied field decreases, this iDW becomes wider (following, approximately, an $H^{-1/2}$ trend [29]), and the Kerr signal decreases smoothly as the iDW width becomes comparable to the layer thickness.

As the field is reduced, Zeeman energy decreases and eventually becomes comparable to iDW energy (σ_w) at a finite positive field H_t. Then, iDW becomes unstable, and there is a sudden reversal of the magnetization in the layer with the lower net magnetic moment. In this process, iDW is annihilated to reduce interfacial exchange energy at the cost of Zeeman energy due to the antiparallel magnetization configuration. In the present case, M_1 is always larger than M_2 (e.g., at 50 K, $M_1 = 1300$ emu/cm^3 and $M_2 = 370$ emu/cm^3, as shown in Fig. 2) so that the transition occurs at Layer 2, the top $Gd_{11}Co_{89}$ layer, as can be seen in Fig. 4. Thus, iDW energy can be estimated from the energy balance between Zeeman and DW energy at the transition as [18]

$$\sigma_w = 2H_t M_2 t_2. \qquad (1)$$

For example, at 50 K, H_t is 1.4 kOe, and $\sigma_w = 5$ erg/cm^2.

At low temperatures, the high field reversible variation of M_2 before this transition is relatively large (down to almost $0.25M_2$ just before H_t) indicating that, at the transition field, iDW width is comparable to Layer 2 thickness. However, as temperature increases, this sharp reversal occurs from an

almost saturated configuration in Layer 2 (e.g., at $0.85M_2$ at 300 K) and with a small coercivity of about 40 Oe.

When the applied field is reversed, the magnetization of Layer 1 (with the larger magnetic moment) is also reversed, carrying along the magnetization of Layer 2 due to the strong interfacial exchange coupling. This is seen as an inverted low field hysteresis in the MOTKE loops of Fig. 4. This process presents an almost temperature independent coercivity of about 30 Oe, which is only slightly larger than the 20 Oe coercive field of the individual $Gd_{35}Co_{65}$ layer [see the loop in Fig. 2(c)].

Finally, as the reversed field increases in magnitude, the Zeeman energy of Layer 2 becomes large enough to overcome interfacial exchange coupling, and there is again a sudden magnetization reversal at $-H_t$ as M_2 becomes parallel to the applied field direction and an iDW is nucleated in the system. This is followed by a smooth decrease of the Kerr signal towards negative saturation as the width of the iDW shrinks under the action of the applied field.

Figures 4(e)–4(g) show the MOTKE loops of the top $Gd_{11}Co_{89}$ layer in a 50 nm $Gd_{35}Co_{65}$/7.5 nm Gd/50 nm $Gd_{11}Co_{89}$ trilayer measured in the 50 K to 200 K temperature range. At low temperatures, the qualitative behavior of the trilayer is very similar to the bilayer with the same three-transitions-loops characteristic of high field iDW nucleation. Comparing the bilayer and trilayer MOTKE loops measured at the same temperature, the main differences are the lower values of the transition fields and the larger magnitude of the magnetization jump at the transition, suggesting a smaller width of iDWs in the trilayer. However, at 200 K, there is a qualitative change in the behavior of the trilayer: only a single low field hysteresis loop is observed in which the magnetization of Layer 2 follows the applied field direction with a 20 Oe coercive field.
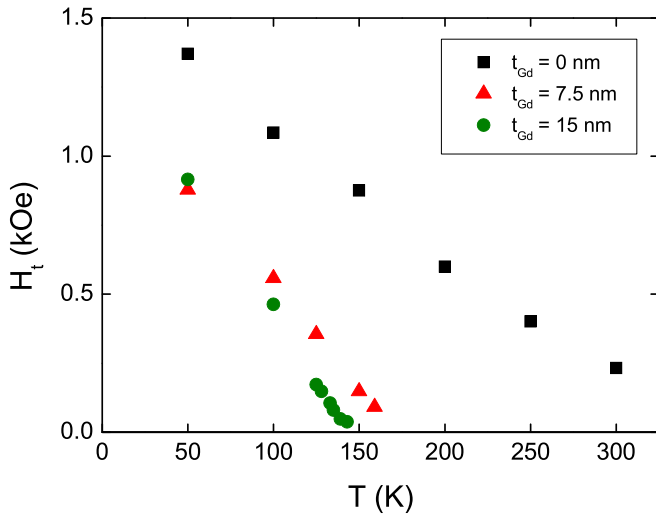
FIG. 5. (Color online) Temperature dependence of transition field in $Gd_{11}Co_{89}/Gd/Gd_{35}Co_{65}$ trilayers.

These differences can be seen in more detail in Fig. 5 where the temperature dependence of the transition field H_t is plotted for the 50 nm $Gd_{35}Co_{65}$/50 nm $Gd_{11}Co_{89}$ bilayer (squares) and two 50 nm $Gd_{35}Co_{65}$/Gd/50 nm $Gd_{11}Co_{89}$ trilayers with $t_{Gd} = 7.5$ nm and 15 nm (triangles and circles, respectively). The presence of the intermediate Gd layer lowers

H_t at all temperatures in comparison with the bilayer. In particular, as T increases, H_t decreases steeply in the trilayers. Eventually, H_t becomes comparable to the coercivity of the low field hysteresis process for T above 160 K and 140 K for $t_{Gd} = 7.5$ nm and 15 nm, respectively. Above this temperature, the top $Gd_{11}Co_{89}$ layer becomes effectively decoupled from the bottom $Gd_{35}Co_{65}$ layer and no signature of iDW nucleation appears during the magnetization reversal process of the multilayer.

B. Magnetization depth profiles

The configuration of iDWs in these Gd-Co multilayers was studied by XRMS at 50 K and different applied fields in order to obtain the magnetization depth profiles. Measurements are performed in the resonant condition at the Gd L_3 edge so that the DW profiles within the Gd ion sublattice will be recovered: as sketched in Fig. 1, the Gd magnetization (M_{Gd}) profiles should change from uniform magnetization at low fields to 180° DW at high fields.

Figure 6 shows the comparison between two typical XRMS asymmetry ratio curves for a 50 nm $Gd_{35}Co_{65}$/50 nm $Gd_{11}Co_{89}$ bilayer for applied fields below and above H_t, i.e., either without or with iDW: In Fig. 6(a), the applied field is 0.2 kOe, well below the transition field at this temperature ($H_t = 1.4$ kOe), whereas the data in Fig. 6(b) correspond to $H = 10$ kOe, much larger than H_t. The main qualitative
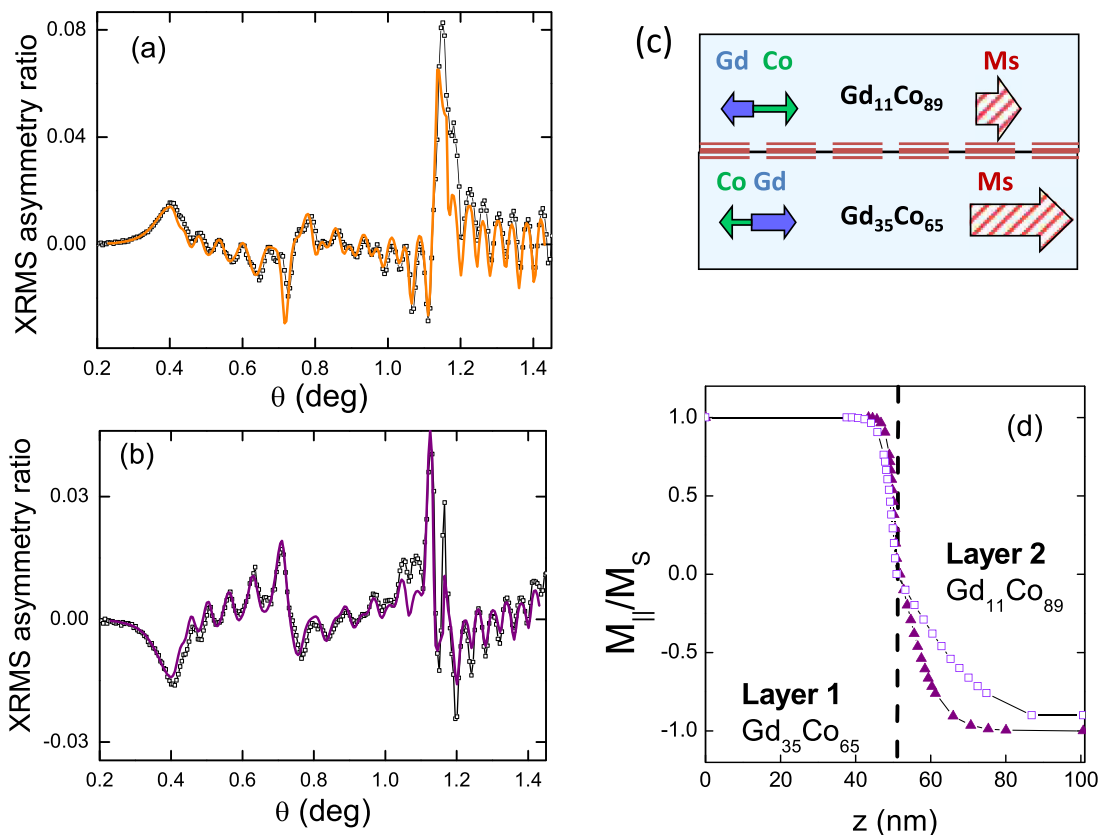

FIG. 6. (Color online) The XRMS asymmetry ratio measured at 50 K for a 50 nm $Gd_{35}Co_{65}$/50 nm$Gd_{11}Co_{89}$ bilayer: (a) $H = 0.2$ kOe, (b) $H = 10$ kOe. Solid lines are fits to obtain magnetization depth profiles. (c) Sketch of high field magnetization configuration of the bilayer with iDW. (d) Fitted magnetization depth profiles at $H = 1.8$ kOe (squares) and $H = 10$ kOe (triangles). Dashed lines indicates interface between $Gd_{35}Co_{65}$ and $Gd_{11}Co_{89}$ layers. Note the asymmetric DW width at both sides of the interface.

difference between these two XRMS curves is the change of sign of the magnetic asymmetry ratio in the low angle range ($\theta < 1.1°$) in the high field curve. Simulations using the PPM XML TENS code [28] show that this sign reversal is a direct signature of the reverse orientation of M_{Gd} in Layer 2, as sketched in Fig. 6(c), and, therefore, of the presence of an iDW in the bilayer, in agreement with the MOTKE characterization.

Now, in order to obtain a quantitative description of the magnetization profile across the iDW, these XRMS asymmetry ratio data have been fitted using the PPM XML TENS code [28] for the analysis of XRMS data in magnetic multilayers. The fitting procedure has been performed in three steps. First, the data at 0.2 kOe (no iDW) have been fitted using, as starting point, the structural information from the fit of the chemical reflectivity curves (see Fig. 3) and assuming a uniform positive magnetization orientation across the whole sample thickness. The layer thicknesses obtained from the fit of the XRMS data are $t_1 = 50.7 \pm 0.4$ nm and $t_2 = 49.7 \pm 0.4$ nm with Gaussian roughness $r_1 = 1.4$ nm and $r_2 = 1.3$ nm, i.e., very similar to the values obtained from the chemical reflectivity fit.

In a second step, the data at fields above H_t (with iDW), either $H = 1.8$ kOe or 10 kOe, have been fitted keeping the structural information constant (i.e., using layer thicknesses and roughness obtained from the previous fit at 0.2 kOe), while the magnetization depth profile was allowed to vary. In order to reduce the number of free parameters, a typical Bloch wall profile was used to describe the gradual M_{Gd} variation across the thickness. In particular, the spatial magnetization variation has been described as

$$M_{||} = M_s \tanh[(z - z_0)/D]$$
$$M_{\perp} = \left[M_s^2 - M_{||}^2\right]^{1/2},$$

$$(2)$$

where $M_{||}$ and $M_{\perp}$ are the in-plane M_{Gd} components either parallel or perpendicular to the field direction, z is the spatial coordinate across the thickness (with $z = 0$ at the bottom of the Gd-Co bilayer), D corresponds to DW width, and z_0 to DW center. This gradual magnetization profile has been discretized into a set of 30 sublayers with constant magnetization given by Eq. (2). The experimental asymmetry ratio has been fitted using, as independent parameters, DW width in each layer (D_1 and D_2) and DW center in each layer ($z_{0,1}$ and $z_{0,2}$). The fit shown in Fig. 6(b) corresponds to $D_1 = 3.4$ nm ± 0.8 nm, $D_2 = 24.0$ nm ± 0.8 nm, $z_{0,1} = 50.9 \pm 0.2$ nm, and $z_{0,2} = 51.0 \pm 1.2$ nm.

Third, as a final consistency check, the XRMS asymmetry ratio at 0.2 kOe has been calculated, again with the same discretization used for iDW description but with uniform magnetization. The quality of the fit with the discretized profile is very similar to that of our initial calculation using just two Gd-Co layers.

In summary, three different fits were performed (for the data at 0.2 kG [no iDW], at 1.8 kOe, and at 10 kOe) using the same structural information and the same discretization. The changes in XRMS response are exclusively the result of different magnetization depth profile: uniform magnetization at 0.2 kOe and iDW with different widths at 1.8 kOe and 10 kOe. The fitted curves are plotted as solid lines in Figs. 6(a) and 6(b) and follow closely the experimental XRMS asymmetry ratio data.

TABLE I. Comparison of DW width, at two different magnetic fields, obtained from XRMS analysis (D_i) in the 50 nm $Gd_{35}Co_{65}$/50 nm$Gd_{11}Co_{89}$ bilayer at 50 K and from analytical model Eq. (4), $\delta_i = \pi/2 * (A_{GdCo}/M_i H)^{1/2}$. Error bars in fitted D values are 0.8 nm.

H (kOe)	D_1 (nm)	D_2 (nm)	δ_1 (nm)	δ_2 (nm)
1.8	3.4	24.0	10.5	20
10	2.2	9.4	4.5	8.4

Figure 6(d) shows the fitted iDW profiles across the bilayer at 1.8 kOe and 10 kOe. In both cases, iDWs appear clearly centered at the structural interface between Layers 1 and 2, i.e., $M_{||}$ is continuous and zero at the interface. This is important since the net magnetization is parallel to M_{Gd} in Layer 1 but antiparallel to it in Layer 2. Thus, the change of sign of M_{Gd} at the interface implies that the net magnetization is always positive across the whole iDW thickness, which minimizes Zeeman energy. This configuration also minimizes interfacial exchange since there is no magnetization jump at the interface.

The DW width is found to be clearly asymmetric at both sides of the structural interface (see Table I). For example, at $H = 1.8$ kOe, M_{Gd} is essentially parallel to the applied field in Layer 1 except in a small region a few nanometers from the interface in which it rotates from $0°$ to $90°$ ($D_1 = 3.4$ nm); in Layer 2, where $D_2 = 24$ nm, the iDW extends across the whole layer thickness, and M_{Gd} turns from $90°$ at the interface to only $150°$ at the upper surface. This is consistent with the MOTKE loop in Fig. 4(a) that shows that at 50 K and 1.8 kOe, the magnetization of Layer 2 is not yet fully saturated.

The observed asymmetry can be ascribed to the different net magnetization in each layer (at 50 K, $M_1 = 1300$ emu/cm^3 and $M_2 = 370$ emu/cm^3) so that the relative weight of Zeeman to exchange energies is different in each layer, resulting in a more gradual spatial variation of M_{Gd} in the Gd-Co alloy with smaller net magnetization. As the field increases up to 10 kOe, DW width decreases steeply in both layers down to $D_1 = 2.2$ nm and $D_2 = 9.4$ nm. This reduction is in agreement with the qualitative behavior expected in these *Re*-TM exchange coupled bilayers [29] and allows the development of a full $0°$ to $180°$ iDW across the bilayer thickness.

Figure 7 shows a similar XRMS characterization for a 50 nm $Gd_{35}Co_{65}$/7.5 nm Gd/50 nm $Gd_{11}Co_{89}$ trilayer at 50 K. The XRMS asymmetry ratio is shown for applied fields below and above $H_t = 0.8$ kG in Figs. 7(a) and 7(b), respectively. Once again, the change of sign of low angle XRMS data provides the first qualitative indication of the presence of an iDW at high fields, as sketched in Fig. 7(c).

Some clear differences were found in the analysis of the trilayer data in comparison with the bilayer, both in the composition and magnetization depth profiles [see Figs. 7(d) and 7(e)]. The low field XRMS asymmetry data of Fig. 7(a) (no iDW and uniform magnetization) were found to be much more sensitive to the structure of the Gd interlayer than the XRMS (charge) reflectivity data. Average layer thicknesses are in agreement with the results of the structural fit (as in the bilayer case), but a good description of the experimental XRMS asymmetry ratio curve was only possible after allowing a certain degree of interdiffusion at the Gd-Co/Gd interfaces.
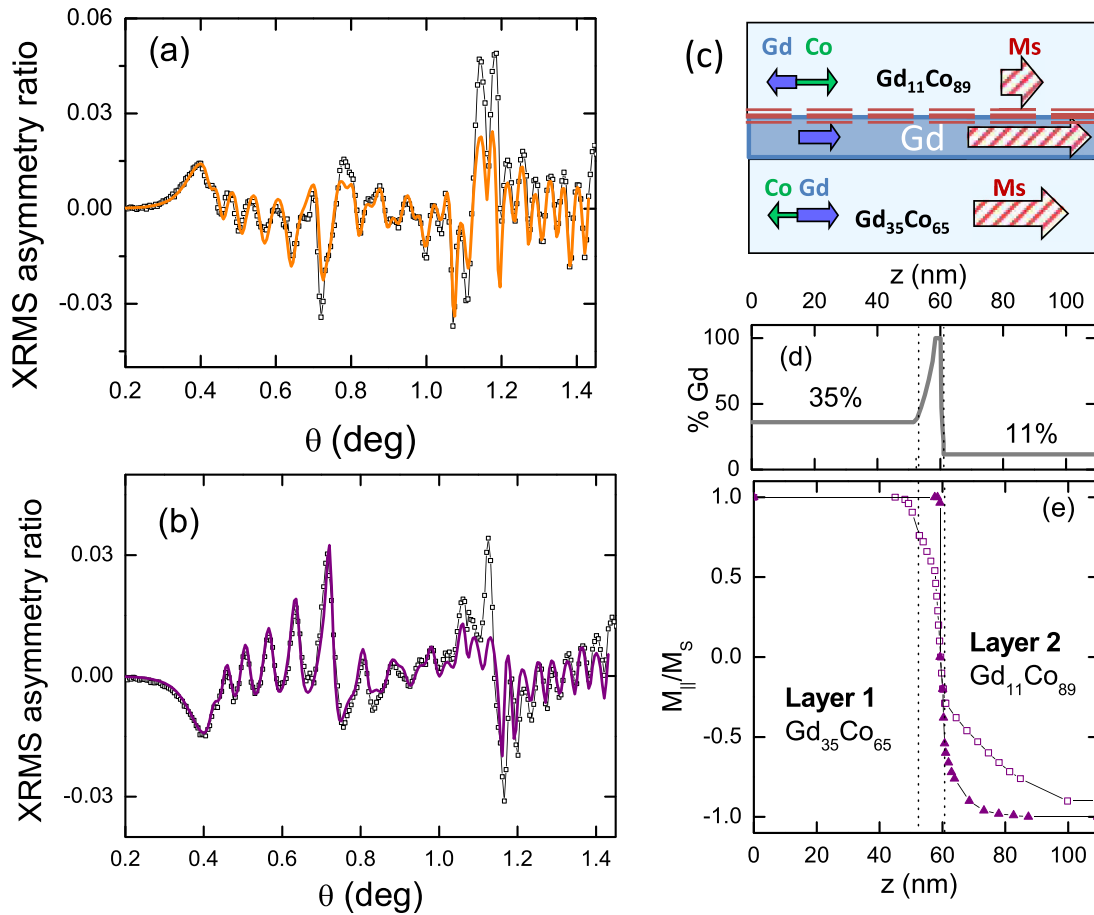
FIG. 7. (Color online) The XRMS asymmetry ratio measured at 50 K at Gd L3 edge with circular polarization for a 50 nm $Gd_{35}Co_{65}$/7.5 nm Gd/50 nm$Gd_{11}Co_{89}$ trilayer at (a) $H = 0.2$ kOe and (b) $H = 10$ kOe. Solid lines are fits to obtain magnetization depth profiles. (c) Sketch of high field magnetization configuration of the trilayer with iDW. (d) Depth dependence of %Gd obtained from the fit of XRMS data at 0.2 kOe (i.e., uniform magnetization profile). Dashed lines indicate the position of the interfaces according to the structural XRMS reflectivity fit. Note the presence of interdiffused Gd-Co regions with variable composition at Gd-Co/Gd interfaces. (e) Fitted magnetization depth profiles at $H = 1.8$ kOe (squares) and $H = 10$ kOe (triangles).

Figure 7(d) shows the spatial variation of Gd ratio (%Gd) across the trilayer derived from the best fit of the data in Fig. 7(a): The interdiffused layer is 5 nm thick at the $Gd_{35}Co_{65}$/Gd interface and 1 nm thick at the $Gd/Gd_{11}Co_{89}$ interface. This is consistent with previous works in Gd/Co thin films [30] and multilayers [23] that have also reported a certain degree of alloying at the interfaces with an asymmetric character due to the different diffusion of Gd on Co than of Co on Gd.

The fit of the high field XRMS asymmetry data, using the obtained structural description of the trilayer, provides the M_{Gd} profiles plotted in Fig. 7(e). Both at $H = 1.8$ kOe and 10 kOe, iDWs are centered at the $Gd/Gd_{11}Co_{89}$ interface so that the condition of positive net magnetization that minimizes Zeeman energy is fulfilled again across the whole trilayer thickness. At both fields, the iDW profile in the trilayer is qualitatively similar. The first 0°–90° rotation in the iDW takes place mostly within the Gd interlayer, followed by a more gradual rotation across Layer 2 ($Gd_{11}Co_{89}$). At $H = 1.8$ kOe, the first 0°–90° rotation occurs over a finite 10 nm width that includes both the pure Gd layer and the interdiffused $Gd_{35}Co_{65}$/Gd interface. $M_{||}/M_S$ is first reduced from 1 down to 0.76 within 5 nm close

to the interface in Layer 1, then, it decreases gradually down to 0.5 within the interdiffused $Gd_{35}Co_{65}$/Gd region. Across the pure Gd layer, $M_{||}/M_S$ then drops sharply down to zero at the $Gd/Gd_{11}Co_{89}$ interface where the net magnetization changes sign relative to M_{Gd}. Finally, M_{Gd} rotates from 90° down to 150° across Layer 2. At $H = 10$ kOe, iDW has shrunk significantly. M_{Gd} stays essentially constant parallel to the applied field across Layer 1 and the Gd interlayer, then, M_{Gd} jumps suddenly to 90° at the $Gd/Gd_{11}Co_{89}$ interface, followed by a fast rotation down to 130° across the 1 nm thick interdiffused interface. Finally, within the homogenous $Gd_{11}Co_{89}$ layer, a more gradual magnetization rotation takes place down to 180° following the Bloch profile of Eq. (2) with effective DW width 9.4 nm, the same as in the bilayer in the same conditions. Total iDW thickness ($M_{||}/M_S$ variation from −0.76 to +0.76) is about 5 nm, in comparison with 12 nm in the bilayer at the same field and temperature.

This fast rotation of the magnetization within the pure Gd layer, observed both at 1.8 kG and 10 kG, is a consequence of the smaller exchange stiffness of Gd and is directly related with the softening of the exchange spring effect found in the MOTKE characterization of the trilayers.

C. Interfacial domain walls

Magnetization profiles in iDWs are determined by the competition between exchange interaction and Zeeman energy, given by the local equilibrium condition [29]

$$2A\,d^2\theta/dz^2 = M_i\,H\sin\theta, \qquad (3)$$

where A is the exchange stiffness, θ is the angle between the local magnetization and the applied field, and M_i is the saturation magnetization of each layer. This simple analytical model can be integrated to obtain the iDW magnetization depth profile [29], depending only on material parameters in each layer of the system and on the angle of the magnetizations at each side of the interface (i.e,. $\theta_{1,\text{int}}$ and $\theta_{2,\text{int}}$ defined at $z = z_{\text{int}}$).

In the original analytical model [29], $\theta_{i,\text{int}}$ was calculated assuming constant $d\theta/dz$ at the interface so that $\theta_{i,\text{int}}$ was a function of M_i and H. However, taking into account the analysis of the XRMS asymmetry ratio curves of the bilayer in Fig. 6, we have considered the experimental condition $\theta_{1,\text{int}} = \theta_{2,\text{int}} = 90°$. In this case, iDW width (δ_i) at the interface can be calculated as

$$\delta_{\text{i}} = \pi/2^*1/[d\theta/dz]z_{-\text{int}} = \pi/2^*(A/M_iH)^{1/2}, \qquad (4)$$

which is different at each side of the interface, in agreement with the fitted magnetization profiles in Fig. 6(d).

Also, iDW energy (σ_w) can be calculated using, as a starting point, the analytical model from Ref. [29] but with a more general 180° iDW configuration with $0°-\theta_{1,\text{int}}$ rotation in Layer 1 and $\theta_{2,\text{int}}-180°$ rotation in Layer 2, as

$$\sigma_{\text{w}} = 2(2AH)^{1/2}\big[\sin(\theta_{1,\text{int}})M_1^{1/2} + \sin(\theta_{2,\text{int}})M_2^{1/2}\big]. \qquad (5)$$

Thus, Eq. (5) can be used to estimate exchange stiffness A_{GdCo} in GdCo bilayers and trilayers by comparing experimental σ_w values (obtained at the transition fields of the MOTKE loops using Eq. [1]) with the predicted analytical dependence in terms of H and M_i, using $\sin(\theta_{1,\text{int}})$ and $\sin(\theta_{2,\text{int}})$ as adjustable parameters in the model.

Figure 8 shows a plot of σ_w vs $H_t^{1/2}[1 \times M_1^{1/2} + 1 \times M_2^{1/2}]$ for the $Gd_{11}Co_{89}/Gd_{35}Co_{65}$ bilayer (squares) in which the experimental condition $\theta_{1,\text{int}} = \theta_{2,\text{int}} = 90°$ extracted from the XRMS analysis has been considered (i.e., $\sin[\theta_{1,\text{int}}] = \sin[\theta_{2,\text{int}}] = \sin[90°] = 1$). A clear linear dependence appears (dashed line) with slope $a = (2.96 \pm 0.06) \times 10^{-3}(\text{erg/cm})^{1/2}$ and intercept $b = -1.02 \pm 0.08\,\text{erg/cm}^2$. According to Eq. (5), $a = 2(2A)^{1/2}$, which corresponds to an effective exchange constant for the alloy layers $A_{\text{GdCo}} = 1.05 \times 10^{-6}\,\text{erg/cm}$. This value is only slightly below pure cobalt ($A_{\text{Co}} = 1.55 \times 10^{-6}\,\text{erg/cm}$ [9]), indicating that exchange within the Co sublattice, which is the strongest exchange term in the Gd-Co alloy, determines iDW configuration. The DW widths δ_i, derived from Eq. (4) with this estimated A_{GdCo}, are shown in Table I, in comparison with experimental D_i values, deduced from the XRMS analysis of the bilayer. The agreement between experimental and estimated values is particularly good in Layer 2 in which the iDW extends over a significant fraction of the layer thickness, allowing a more precise determination of the magnetization profile from XRMS curves.
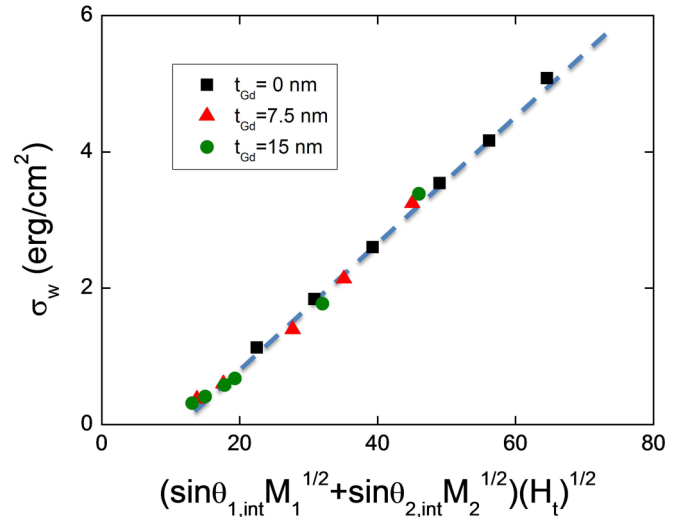

FIG. 8. (Color online) iDW energy calculated as $\sigma_{\text{w}} = 2H_tM_2t_2$ from MOTKE loops in comparison with analytical model Eq. (5). Different $\theta_{i,\text{int}}$ values are used for each sample in order to obtain the scaling of the experimental data to a single line: $\sin\theta_{1,\text{int}} = \sin\theta_{2,\text{int}} = 1$ in $Gd_{11}Co_{89}/Gd_{35}Co_{65}$ bilayer and $\sin\theta_{1,\text{int}} = 0.8$, $\sin\theta_{2,\text{int}} = 1$ in $Gd_{11}Co_{89}/Gd/Gd_{35}Co_{65}$ trilayers. Dashed line is a linear fit of σ_{w} vs $(H_t)^{1/2}[\sin(\theta_{1,\text{int}})M_1^{1/2} + \sin(\theta_{2,\text{int}})M_2^{1/2}]$, according to Eq. (5). Its slope corresponds to exchange stiffness $A_{\text{GdCo}} = 1.05 \times 10^{-6}\,\text{erg/cm}$.

An unexpected result of the linear fit in Fig. 8 is the small negative intercept $b = -1.02 \pm 0.08\,\text{erg/cm}^2$, suggesting a negative interfacial exchange energy. This value is of the same order of magnitude as in other Re-TM alloy multilayers such as Gd-Fe [31] and could be related to the composition change at the interface and the long range nature of exchange interactions in Re-TM systems [32].

A similar analysis has been performed of the field dependence of iDW energy for two $Gd_{11}Co_{89}/Gd/Gd_{35}Co_{65}$ trilayers with different interlayer thickness (see triangles [$t_{\text{Gd}} = 7.5\,\text{nm}$] and circles [$t_{\text{Gd}} = 15\,\text{nm}$] in Fig. 8). It is found that the trilayer data can be scaled with the linear dependence obtained for the bilayer with the same slope (i.e., the same effective exchange constant A_{GdCo}) by changing just the magnetization angles at the interface $\theta_{1,\text{int}}$. In particular, the scaling shown in Fig. 8 corresponds to a reduced magnetization rotation at Layer 1 ($\sin\theta_{1,\text{int}} = 0.8$) keeping ($\sin\theta_{2,\text{int}} = 1$). This result is consistent with the magnetization profiles obtained in Fig. 7 from the XRMS data in the trilayer in which a clear reduction of the magnetization rotation angle at the interface was observed only within Layer 1 but not in Layer 2. For example, at $H = 1.8\,\text{kG}$, $M_{||}/M_S = \cos\theta_1$ varies between 0.76–0.5 at the $Gd_{35}Co_{65}/Gd$ interface (i.e., $\sin\theta_{1,\text{int}}$ should be in the range 0.65–0.85), whereas at the $Gd/Gd_{11}Co_{89}$ interface $\theta_{2,\text{int}}$ remains at 90°.

Also, the scaling between bilayer and trilayer DW energies using Eq. (5) without any additional term for the Gd interlayer suggests that, at a given field, the contribution to the total σ_{w} from the magnetization rotation within the pure Gd layer is negligible, in agreement with the much smaller exchange interactions in Gd than in Co [23].

Thus, the main role of the Gd interlayer in the magnetic behavior of the trilayer system is to provide a low exchange region at the iDW center ferromagnetically coupled to Layer 1 into which the central part of iDW shifts. This reduces the amount of magnetization rotation within Layer 1 and, consequently, its contribution to total iDW energy (proportional to $\sin(\theta_{1,\text{int}})M_1^{1/2}$) without adding any significant DW energy contribution from the rotation that takes place within the Gd layer. This σ_w reduction translates into lower transition fields for the nucleation of the spring magnet configuration.

IV. CONCLUSIONS

In summary, iDWs have been studied in $Gd_{35}Co_{65}/Gd/Gd_{11}Co_{89}$ trilayers with Gd thickness in the 0–15 nm range by combined MOTKE and XRMS measurements. The presence of a Gd interlayer in the system results in a clear weakening of exchange coupling between the top and bottom Gd-Co layers: The fields needed for iDW nucleation are smaller in the trilayers than in the bilayer, and the spring-magnet effect becomes restricted to a lower temperature range. Magnetization profiles derived from XRMS measurements show that iDWs are centered at the bilayer interface but with asymmetric width (narrower in the high magnetization $Gd_{35}Co_{65}$ layer

and broader in the low magnetization $Gd_{11}Co_{89}$ layer). The largest fraction of iDW energy corresponds to 0°–90° rotation of the magnetization within the narrow wall localized in Layer 1 ($Gd_{35}Co_{65}$). In the trilayers, due to the ferromagnetic alignment between $Gd_{35}Co_{65}$ layer and the Gd interlayer, iDWs shrink and shift from the lower $Gd_{35}Co_{65}$ layer into the Gd interlayer. This reduces the amount of magnetization rotation within the high magnetization $Gd_{35}Co_{65}$ layer. As a consequence, iDW energy decreases, and coupling between the upper $Gd_{11}Co_{89}$ and lower $Gd_{35}Co_{65}$ layers weakens due to the much smaller Gd-Gd than Co-Co exchange interactions.

[1] S. Mangin, M. Gottwald, C-H. Lambert, D. Steil, V. Uhlíř, L. Pang, M. Hehn, S. Alebrand, M. Cinchetti, G. Malinowski, Y. Fainman, M. Aeschlimann, and E. E. Fullerton, Nature Materials **13**, 286 (2014).

[2] S. Romer, M. A. Marioni, K. Thorwarth, N. R. Joshi, C. E. Corticelli, H. J. Hug, S. Ozer, M. Parlinska-Wojtan, and H. Rohrmann, Appl. Phys. Lett. **101**, 222404 (2012).

[3] A. López-Ortega, M. Estrader, G. Salazar-Alvarez, S. Estradé, I. V. Golosovsky, R. K. Dumas, D. J. Keavney, M. Vasilakaki, K. N. Trohidou, J. Sort, F. Peiró, S. Suriñach, M. D. Baró, and J. Nogués, Nanoscale **4**, 5138 (2012).

[4] A. Hierro-Rodriguez, J. M. Teixeira, M. Vélez, L. M. Alvarez-Prado, J. I. Martín, and J. M. Alameda, Appl. Phys. Lett. **105**, 102412 (2014).

[5] R. Morales, A. C. Basaran, J. E. Villegas, D. Navas, N. Soriano, B. Mora, C. Redondo, X. Batlle, and I. K. Schuller, Phys. Rev. Lett. **114**, 097202 (2015).

[6] T. Hauet, F. Montaigne, M. Hehn, Y. Henry, and S. Mangin, Appl. Phys. Lett. **93**, 222503 (2008).

[7] A. Yu. Dobin and H. J. Richter, Appl. Phys. Lett. **89**, 062512 (2006).

[8] T. N. Anh Nguyen, R. Knut, V. Fallahi, S. Chung, Q. T. Le, S. M. Mohseni, O. Karis, S. Peredkov, R. K. Dumas, C. W. Miller, and J. Åkerman, Phys. Rev. Appl. **2**, 044014 (2014).

[9] C. Eyrich, A. Zamani, W. Huttema, M. Arora, D. Harrison, F. Rashidi, D. Broun, B. Heinrich, O. Mryasov, M. Ahlberg, O. Karis, P. E. Jönsson, M. From, X. Zhu, and E. Girt, Phys. Rev. B **90**, 235408 (2014).

[10] B. Li, R. V. Chopdekar, E. Arenholz, A. Mehta, and Y. Takamura, Appl. Phys. Lett. **105**, 202401 (2014).

[11] G. B. G. Stenning, G. J. Bowden, P. A. J. de Groot, G. van der Laan, A. I. Figueroa, P. Bencok, P. Steadman, and T. Hesjedal, Phys. Rev. B **91**, 094403 (2015).

[12] Y. Liu, S. G. E. te Velthuis, J. S. Jiang, Y. Choi, S. D. Bader, A. A. Parizzi, H. Ambaye, and V. Lauter, Phys. Rev. B **83**, 174418 (2011).

[13] C. J. Aas, P. J. Hasnip, R. Cuadrado, E. M. Plotnikova, L. Szunyogh, L. Udvardi, and R. W. Chantrell, Phys. Rev. B **88**, 174409 (2013).

[14] S. Mukherjee, W. Kreuzpaintner, J. Stahn, J.-G. Zheng, A. Bauer, P. Böni, and A. Paul, Phys. Rev. B **91**, 104419 (2015).

[15] A. D. Naylor, G. Burnell, and B. J. Hickey, Phys. Rev. B **85**, 064410 (2012).

[16] B. Sanyal, C. Antoniak, T. Burkert, B. Krumme, A. Warland, F. Stromberg, C. Praetorius, K. Fauth, H. Wende, and O. Eriksson, Phys. Rev. Lett. **104**, 156402 (2010).

[17] B. Dieny, D. Givord, J. M. B. Ndjaka, and J. M. Alameda, J. Appl. Phys. **67**, 5677 (1990).

[18] R. Morales, J. I. Martín, and J. M. Alameda, Phys. Rev. B **70**, 174440 (2004).

[19] R. Hasegawa, J. Appl. Phys. **46**, 5263 (1975).

[20] R. Zárate, J. I. Martín, A. Pérez-Junquera, M. Vélez, C. Meny, and J. M. Alameda, Phys. Stat. Sol. A **203**, 1431 (2006).

[21] C. Dehesa-Martínez, L. Blanco-Gutiérrez, M. Vélez, J. Díaz, L. M. Alvarez-Prado, and J. M. Alameda, Phys. Rev. B **64**, 024417 (2001).

[22] K. Sato and Y. Togami, J. Magn. Magn. Mater. **35**, 181 (1983).

[23] J. P. Andrés, L. Chico, J. Colino, and J. M. Riveiro, Phys. Rev. B **66**, 094424 (2002).

[24] C. Kittel, *Introduction to Solid State Physics* (Wiley, New York, 1996), p. 466.

[25] D. Haskel, G. Srajer, J. C. Lang, J. Pollmann, C. S. Nelson, J. S. Jiang, and S. D. Bader, Phys. Rev. Lett. **87**, 207201 (2001).

[26] E. Kravtsov, D. Haskel, S. G. E. te Velthuis, J. S. Jiang, and B. J. Kirby, Phys. Rev. B **79**, 134438 (2009).

[27] B. L. Henke, E. M. Gullikson, and J. C. Davis, Atomic Data and Nuclear Data Tables **54**, 181 (1993).

[28] M. Sacchi and A. Mirone, Phys. Rev. B **57**, 8408 (1998); http://www.esrf.eu/Instrumentation/software/data-analysis/OurSoftware/PPM.

[29] B. Dieny, D. Givord, and J. M. B. Ndjaka, J. Magn. Magn. Mat. **93**, 503 (1991).

[30] C. Quirós, I. Popa, O. Robach, D. Wermeille, J. Díaz, R. Felici, and S. Ferrer, Phys. Rev. B **78**, 195406 (2008).

[31] T. Hauet, F. Montaigne, M. Hehn, Y. Henry, and S. Mangin, Phys. Rev. B **79**, 224435 (2009).

[32] J. L. Prieto, M. G. Blamire, and J. E. Evetts, Phys. Rev. Lett. **90**, 027201 (2003).